Liu *et al. Biochar* (2023) 5:31
https://doi.org/10.1007/s42773-023-00231-z

Biochar

ORIGINAL RESEARCH Open Access

Constructing coconut shell biochar/MXenes composites through self-assembly strategy to enhance U(VI) and Cs(I) immobilization capability

Fenglei Liu[1,2], Shanshan Wang[1], Chaofeng Zhao[3] and Baowei Hu[1*]

Abstract

Herein, a biochar-based composite ($Ti_3C_2T_x$@biochar-PDA/PEI) was constructed by decorating $Ti_3C_2T_x$ and polydopamine on coconut shell biochar via electrostatic self-assembly method. Different characterization techniques were applied to explore the structure, morphology and composition of the sorbents. It was found that the higher porosity and diverse functional groups were conducive for $Ti_3C_2T_x$@biochar-PDA/PEI to capture radionuclides, and the water environmental conditions made a great contribution to the adsorption process. The process of removing U(VI)/Cs(I) well complied with the Langmuir isotherm and Pseudo-second-order equations, which indicated that the single layer chemical adsorption occurred on the solid liquid interface. Meanwhile, this produced composite exhibited superior removal performance under complex co-existing ion environment, and the maximum adsorption amounts of U(VI) and Cs(I) reached up to 239.7 and 40.3 mg g^{-1}. Impressively, this adsorbent still exhibited good adsorption performance after three cycles of regeneration. The spectral analysis and DFT calculation demonstrated that adsorption of U(VI) might be a chemical process, while the adsorption of Cs(I) should be ion exchange or electrostatic attraction. This study demonstrated the potential application of $Ti_3C_2T_x$@biochar-PDA/PEI as an effective remediation strategy for radioactive wastewater cleanup.

Highlights

- A coconut shell biochar-based composite was successfully constructed.
- Modified biochar exhibited excellent adsorption ability for U(VI)/Cs(I).
- Removal process of U(VI)/Cs(I) was mainly controlled by chemical adsorption.
- Elimination mechanism was associated with ion exchange and chelation.

Keywords Biochar, MXene, Adsorption, U(VI), Cs(I)

Handling editor: Wenfu Chen

*Correspondence:
Baowei Hu
hbw@usx.edu.cn
Full list of author information is available at the end of the article

Graphical Abstract

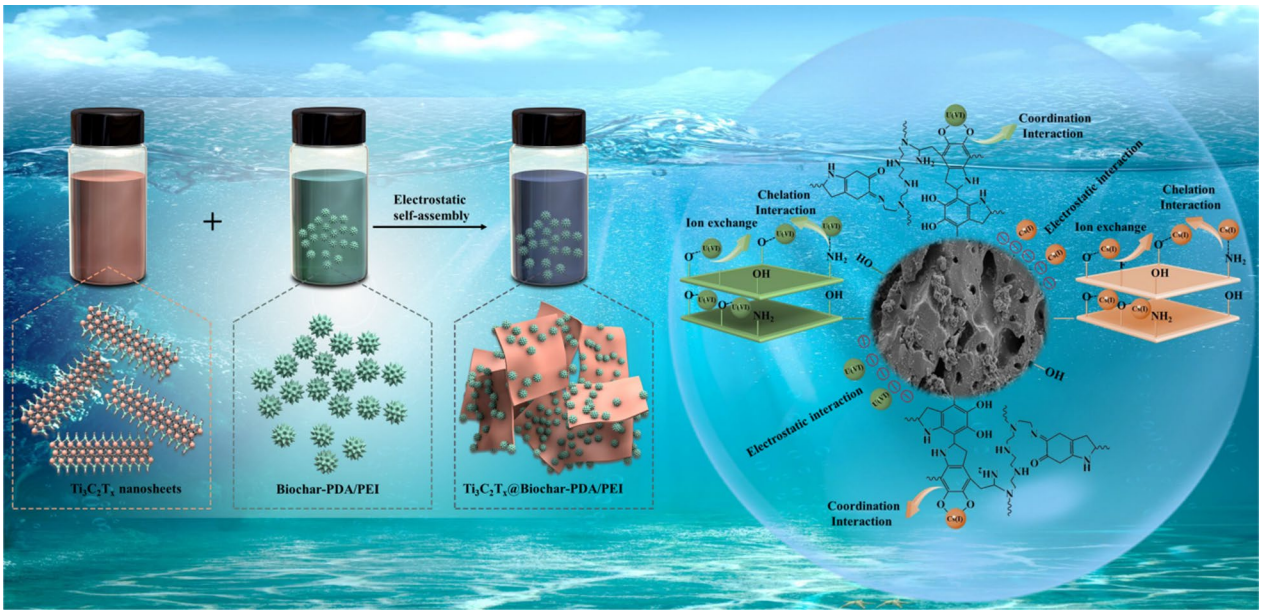

1 Introduction

With the rapid development of nuclear power, a large number of radioactive wastewater is released into the surrounding environment, which has caused a serious threat to the environment and public health (Liu et al. 2019). Among various radionuclides, uranium (U) and cesium (Cs) have attracted considerable research attention due to their high radioactivity, toxicity and solubility (Hu et al. 2022). Thus, it is of vital significance to adsorb and separate of U(VI) and Cs(I) from radioactive wastewater. In response to the environmental problem, many methods have been widely reported to remove emerging pollutants from aqueous solutions, such as liquid–liquid extraction (Xu et al. 2023), chemical precipitation (Yu et al. 2022), electrochemical treatment (Liu et al. 2023) and adsorption (Zhu et al. 2022). Among them, adsorption is deemed to be an effective method for treating contaminated water due to its simplicity and low power consumption (Zheng et al. 2021). Currently, a wide range of alternative adsorbents have been investigated to eliminate these pollutant species, including graphene oxide (Liu and Wang 2020), polymer (Zhang et al. 2010), chitosan (Lu et al. 2021) and montmorillonite (Xia et al. 2018). However, the above-mentioned adsorbents exhibited some shortcomings under different environmental conditions, such as time consuming, high cost and complex process. Thus, it is very much essential to design and construct novel adsorption materials for efficient separation and purification of radionuclides from wastewater.

Biochars are a pyrogenic carbon material derived from renewable biomass, which have attracted more and more attention in the environmental field due to their low cost, abundant source and environmental-friendly (Han et al. 2022). However, pristine biochar from pyrolysis or gasification is relatively poor in surface functional groups and low in porosity, which may affect its adsorption performance and reduce its adsorption application value (Lu et al. 2022). To overcome these problems, synthesis of novel functionalized biochar with surface modification strategy to improve its removal efficiency and potential applications in environmental remediation has attracted much attention in recent years (Fang et al. 2022). For examples, Wang et al. (2020a; b, c) reported that the grafting of amino groups on porous biochar could enhance the adsorption efficiency toward U(VI), and the complexation between U(VI) and amine groups contributed to U(VI) adsorption. Guo et al. (2022) used 3D ZnO modified biochar-based hydrogels for U(VI) elimination, which was easily regenerated and quickly separated after adsorption. Asada et al. (2021) reported a biochar-immobilized potassium nickel hexacyanoferrate adsorbent with excellent Cs(I) removal efficiency, which could effectively extract Cs(I) from nuclear waste. Tao et al. (2019) found that copper hexacyanoferrate

nanoparticle-decorated biochar exhibited a good performance on sedimentation and Cs(I) removal, and the Cs(I) adsorption was homogenous, endothermic and mainly controlled by chemical adsorption. Nevertheless, there are several weaknesses associated with these biochar-based materials, such as low adsorption efficiency, weak selectivity and poor regenerability. Thus, effective modification of biochar-based materials with excellent removal efficiency for radioactive contaminant is still necessary.

MXenes are an emerging class of 2D material and composed of transition metals and carbides, nitrides, or carbonitrides, which are synthesized from the parent MAX phase by selectively removing "A" elements (Zhang et al. 2023). Their specific structure brings about unique and excellent physical and chemical properties, such as high degree of physico-chemical stability, compositional flexibility and ion exchange ability. More importantly, MXenes exhibit a high specific surface area and have a large number of -OH, -F and other oxygen-containing groups on the skeleton. Thus, the theoretical calculations and experiments demonstrated that MXenes exhibited excellent adsorption properties for different contaminants due to its abundant active sites, which have been widely used in the environmental-remediation field (Wang et al. 2018). Dopamine is a biological molecule containing catechol and amine functional groups in its skeleton, and its special chemical structure will facilitate metal coordination and electron transport. More importantly, the oxidative polymerization of the dopamine would take place in aerated alkaline solution, and the coating could be versatilely deposited onto a variety of materials (Liu et al. 2021). Thus, combination of these advantages may be an effective strategy to develop a novel biochar-based sorbent for radioactive wastewater remediation.

Herein, a biochar-based composite was developed by convenient self-assembly for radionuclide elimination. The purpose of this research was (1) to determine the structure, composition as well as morphology of the as-prepared materials by different spectroscopic technologies; (2) to explore the influence of water environmental condition on removal performance of $Ti_3C_2T_x$@biochar-PDA/PEI by batch techniques; (3) to understand the relationship between structure and removal properties through classical kinetics, isotherms and thermodynamic formulas; (4) to evaluate the regeneration ability of $Ti_3C_2T_x$@biochar-PDA/PEI by adsorption–desorption cycle experiments; (5) to research in depth the capture mechanisms of biochar-based composites for U(VI) and Cs(I) through characterization analysis and theoretical calculation. The highlight of this study was to apply this biochar-based composite to the adsorption and immobilization of radioactive pollutants in aqueous solution in actual environmental cleanup.

2 Materials and methods

2.1 Materials and chemicals

The coconut shell biochar, Ti_3AlC_2 (98%), CsCl (99.9%), $UO_2(NO_3)_2.6H_2O$ (99%) and polyethyleneimine (PEI, 99%) were purchased from Beijing Daxiang Chemical Reagent Factory. The HF (98%), tris (hydroxymethyl) aminomethane (Tris, 99.8%), dopamine hydrochloride (98%) and Arsenazo III (AR) were bought from Shanghai Aladdin Biochemical Technology Co., Ltd. All the reagents were of analytical pure grade without further purification.

2.2 Synthesis of Ti_3C_2@biochar-PDA/PEI

The synthetic route for $Ti_3C_2T_x$@biochar-PDA/PEI is illustrated in Fig. 1, and the detailed preparation procedure was according to references with minor modification (Gao et al. 2022; Zhang et al. 2022). Firstly, 5 g of Ti_3AlC_2 powder and 30 mL of HF solution (40 wt%) were added into a 500 mL three-round bottom flash under stirring for 48 h. Then, the mixture was washed with ultrapure water several times until the pH reached neutral to obtain the multilayer $Ti_3C_2T_x$ powder. Subsequently, the resulting $Ti_3C_2T_x$ was centrifuged and sonicated at room temperature to construct monolayer $Ti_3C_2T_x$ nanosheets. Secondly, 2 g of dried biochar and 3 g of PEI were put together into a round bottom flask. Thereafter, 400 mL of dopamine solution was added into the above mixture, followed by vigorous stirring for 24 h to achieve reddish brown precipitation (biochar-PDA/PEI). Thirdly, a negatively charged $Ti_3C_2T_x$ suspension was added into the positively charged amine functionalized biochar dispersion at pH = 6, followed by ultrasonication for 6 h at room temperature. Finally, the obtained sediment was freeze-dried for 24 h to get $Ti_3C_2T_x$@biochar-PDA/PEI.

2.3 Characterization

Surface morphologies and chemical composition of all the adsorbents were observed by scanning electron microscopy (SEM, Merlin Compact, Japan) and high-resolution electron microscopy (TEM, Hitachi, Japan). The pore structure and the specific surface of the sorbents were characterized by nitrogen adsorption–desorption (Autosorb iQ instrument, Quan-tachrome, USA). FTIR analysis was done using Thermo NICOLET 5700 spectrophotometer taking KBr as a reference. Powder X-raydiffraction (WAXRD) patterns were recorded by D8 ADVANCE X-ray diffraction spectrometer (Bruker, German). The X-ray photoelectron analysis was performed by Thermo Scientific ESCALAB 250Xi spectrometer.

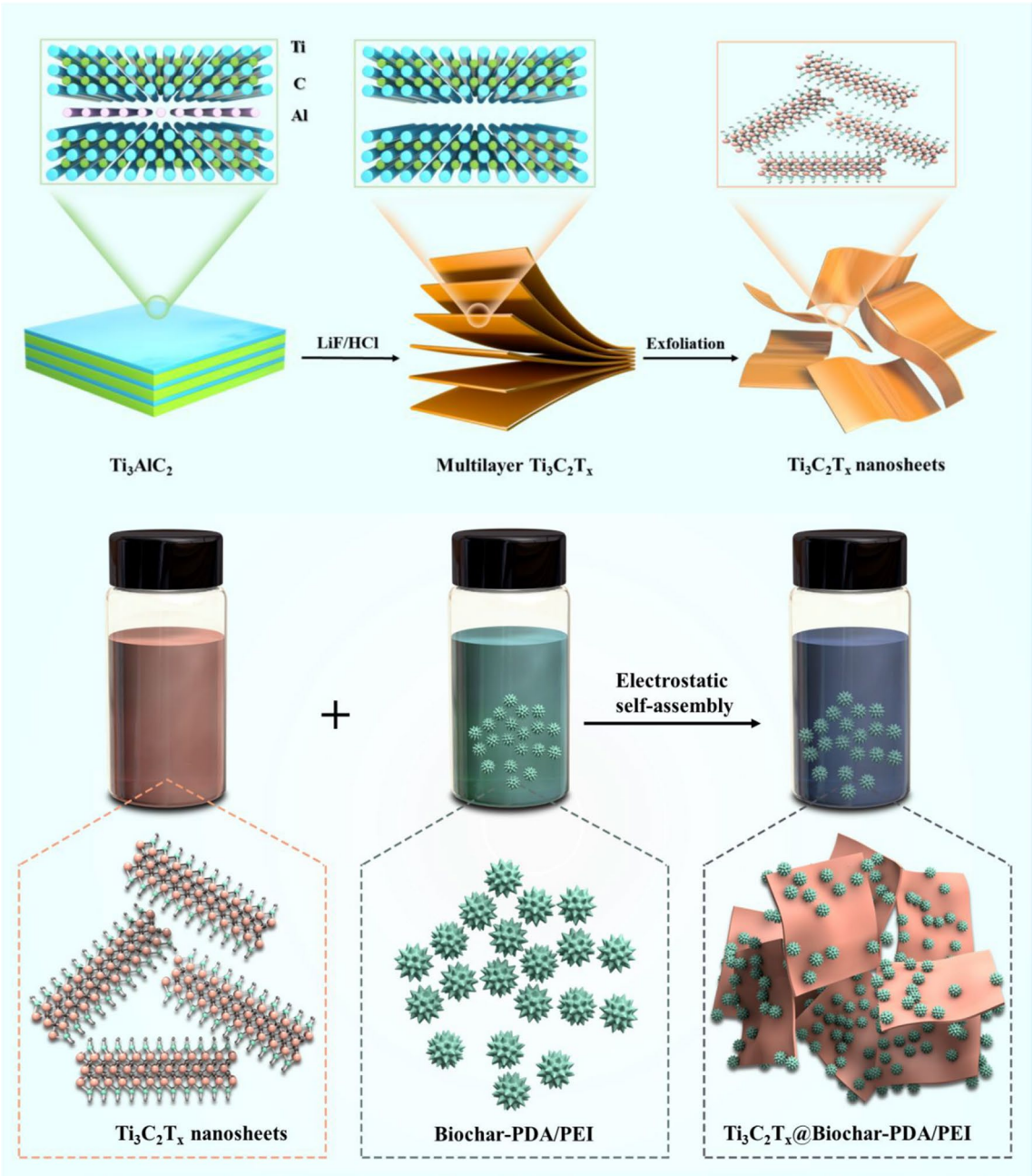

Fig. 1 Schematic illustration for the synthesis process of $Ti_3C_2T_x$@biochar-PDA/PEI

2.4 Batch removal experiments

A batch technique was used to study the applicability of $Ti_3C_2T_x$@biochar-PDA/PEI for adsorbing target metal ions. In the removal system, a fixed amount (5 mg) of $Ti_3C_2T_x$@biochar-PDA/PEI was immersed in the 50 mL of U(VI) or Cs(I) containing solution, in which the pH values were controlled by 0.1 M HCl and 0.1 M NaOH. After adsorption equilibrium, the residual pollutant concentration was quantified by atomic absorption spectrophotometer and UV–vis adsorption spectrometer. To understand the kinetics of the elimination process, 5 mg of sorbent was added to 50 mL of U(VI) and Cs(I) solution, and the liquid supernatant was taken out and the absorbance was measured at different adsorption time. For adsorption isotherm studies, a moderate amount of adsorbent was dropped into 50 mL of different concentrations of radionuclide solution, which was vibrated at constant temperature for a certain time. The

adsorbents were regenerated for three cycles by the consecutive adsorption–desorption process described above. Finally, the equilibrium absorption capacity (q_e mg g^{-1}) and removal efficiency (R_e %) were calculated in terms of Eq. (1) and (2):

$$q_e = \frac{(C_o - C_t)V}{m} \quad (1)$$

$$R_e = \frac{C_o - C_t}{C_o} \times 100\% \quad (2)$$

where C_0 and C_e (mg L^{-1}) arethe initial and equilibrium concentrations in clear liquor before and after sorption. V represents the volume of pollutant solution (L), and m is the mass of samples (mg).

3 Results and discussion

3.1 Adsorbent characterization

The change in different surface functional groups on all the adsorbents was examined by FTIR spectra, and the obtained results are showed in Fig. 2a. For original biochar, a moderate peak around at 3428 cm^{-1} represented the stretching vibration of O–H, and a band at 1638 cm^{-1} was consistent with C=O stretching vibration (Dong et al. 2021). The peaks at about 1430 cm^{-1} and 1085 cm^{-1} would be assigned to the C–H and C–O bending vibrations, respectively. However, for biochar-PDA/PEI, it was found that the intensity of peaks for −OH and C=O significantly increased after surface modification, which may be due to the introduction of PDA and PEI on the surface (Liu et al. 2022). The FTIR spectra of $Ti_3C_2T_x$ exhibited two typical characteristic peaks at 3443 and 549 cm^{-1}, which indicated that a large amount of -OH and Ti–OH groups existed on the surface of MXenes (Hu et al. 2021). It was noted that the $Ti_3C_2T_x$@biochar-PDA/PEI showed the characteristic peaks of biochar, PDA and $Ti_3C_2T_x$, such as the stretching vibration of C-Ti, C=O and $-NH_2$ matching with the peaks in the range of 556 cm^{-1}–1623 cm^{-1}. These phenomena reflected that this biochar-based composite was successful constructed and it contained abundant amino and oxygen-containing groups. In Fig. 2b, one can see that the peaks of C1s, O1s, Al2p and Ti2p are found in Ti_3AlC_2, while the $Ti_3C_2T_x$ mainly consists of C1s, O1s and Ti2p, which may be due to the successful removal of Al elements by HF solution. The obvious N1s signals were observed in the XPS spectra of biochar-PDA/PEI compared with biochar, which indicated that PDA/PEI was a good precursor to introduce amino groups. More importantly, the survey scan XPS profiles revealed the presence of C1s, O1s, N1s and Ti2p elements in $Ti_3C_2T_x$@biochar-PDA/PEI. Besides, to analyze the surface functional groups of the samples in depth, the peaks of C1s were further deconvolved in this work. In Fig. 2c, the biochar shows three C1s peaks at 283.5 eV, 285.4 eV and 289.1 eV corresponding to C–C, C–O and C=O groups. In comparison to biochar, a new peak at 284.9 eV (C–NH_2) was induced in the C1s spectra of biochar-PDA/PEI (Fig. 2d), which may be caused by the amine groups immobilized on the surface of biochar. In Fig. 2e, the $Ti_3C_2T_x$@biochar-PDA/PEI exhibits five different C1s peaks at 284.2 eV (C–C), 286.1 eV (C–O), 288.1 eV (C=O), 285.2 eV (C–NH_2) and 283.1 eV (C–Ti), and the existence of C-Ti and C-NH_2 implied that MXenes and PDA/PEI were successfully anchored on biochar. Besides, the XRD analysis was also carried out to evaluate the crystal structure of the as-prepared sorbents. In Fig. 2f, the XRD patterns of biochar present broad amorphous features and no peaks indicative of crystalline phases. However, the XRD pattern of Ti3C2Tx exhibited an obvious diffraction peak (002) at a lower angle ($2\theta = 5.93°$), which was an indicative of enlarged interlayer spacing and the layered structure appeared without impurity phase (Peng et al. 2022). After electrostatic self-assembly, the (002) reflection peak disappeared and the intensity of the (004) peak became weak, which implied that the disorder of MXenes layers increased due to some chemical reactions occurred in MXenes sheets.

The microstructures and surface morphologies of the as-prepared adsorbent were further characterized by means of SEM and TEM technologies. In Fig. 3a, one can see that the coconut shell biochar exhibits fine granular particles, and its surface is the smooth and porous in structure (Sun et al. 2022). In contrast, the biochar-PDA-PEI (Fig. 3b) presented a relatively rough surface that had experienced obvious erosion, and substantial pore channels were blocked by macromolecular organic matter. Interestingly, in Fig. 3c, some sheet structures that distributed on the surface of $Ti_3C_2T_x$@biochar-PDA/PEI are found, which may be attributed to the attachment of $Ti_3C_2T_x$ nanosheets onto the surface of biochar by electrostatic self-assembly. Moreover, in Fig. 3d, the TEM image of $Ti_3C_2T_x$@biochar-PDA/PEI composite reveals uniformly distributed flake-like nano-structures and porous structures, which suggests the effectiveness of the synthesis method herein to produce a biochar-based composite. Figure 3e, f show the N_2 adsorption–desorption isotherms and pore size distributions of coconut shell biochar and the corresponding samples functionalized with PDA/PEI and MXenes. It was found that all samples showed type-IV adsorption isotherm, which was the typical characteristic of mesoporous materials (Cheng et al. 2022). Additional file 1: Table S1 shows that the surface areas of biochar, biochar-PDA-PEI and $Ti_3C_2T_x$@biochar-PDA/PEI were 778.1, 72.7 and 51.6 m^2 g^{-1}, respectively. The BET surface area of biochar-PDA-PEI

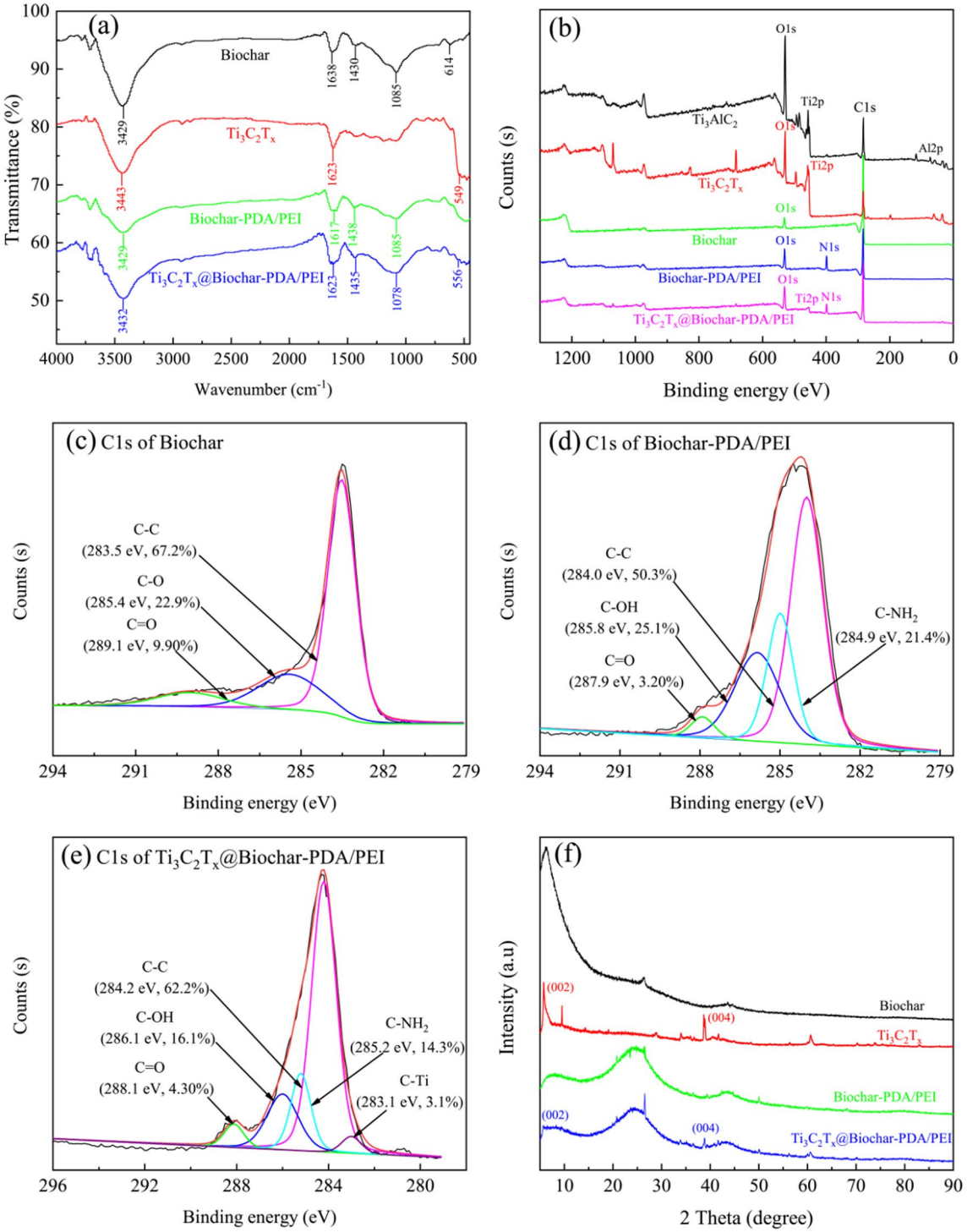

Fig. 2 FTIR spectra (**a**), XPS survey spectra (**b**), high-resolution C1s (**c**–**e**) and XRD patterns (**f**) of biochar, $Ti_3C_2T_x$, biochar-PDA-PEI and $Ti_3C_2T_x$@biochar-PDA/PEI

and $Ti_3C_2T_x$@biochar-PDA/PEI was lower than that of biochar, possibly because PDA/PEI and $Ti_3C_2T_x$ occupied a great many of porous channels. However, the average pore diameter exhibited an increasing trend, which may be due to that fact that small pores were firstly filled and then the large pores. It should be pointed out that the

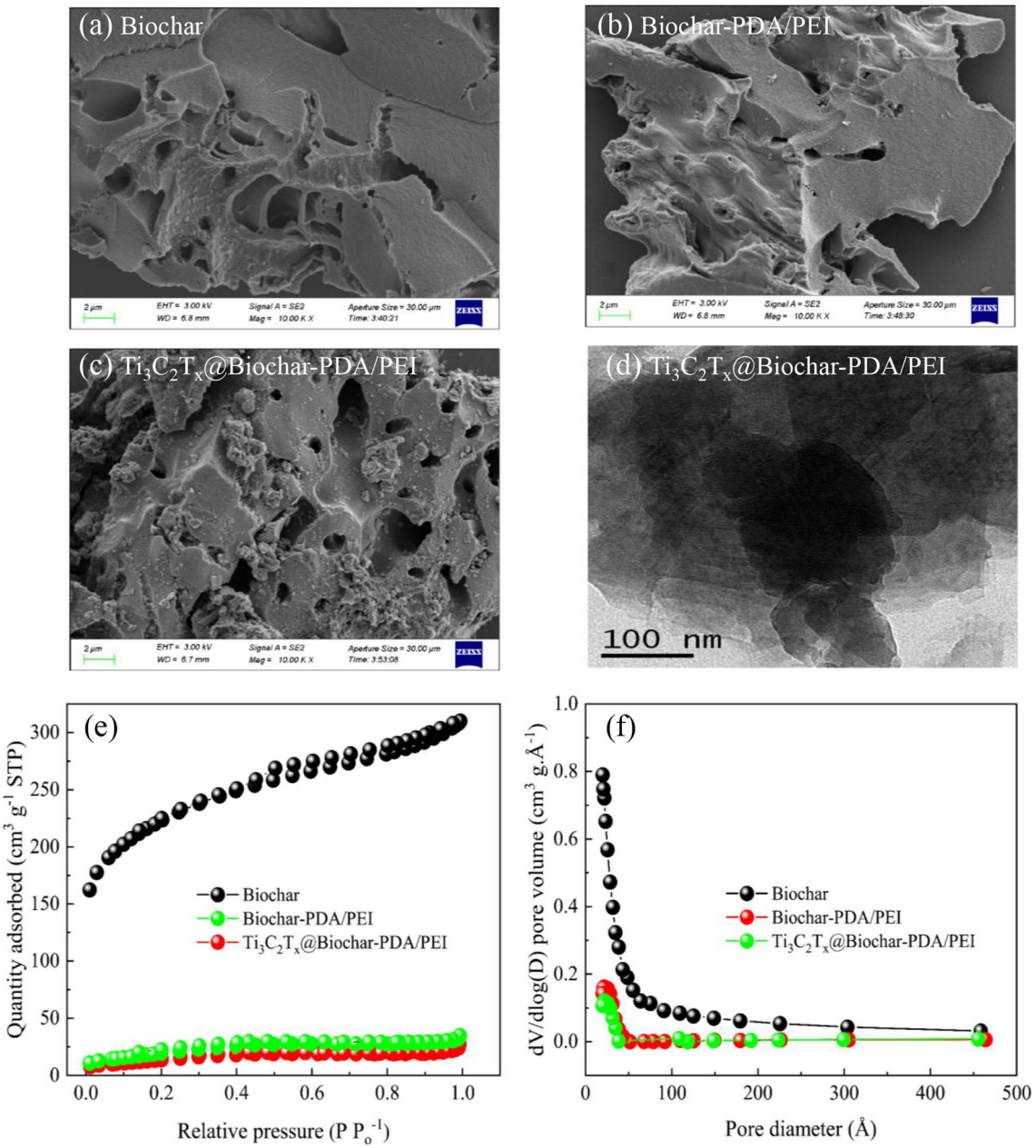

Fig. 3 SEM image (**a**–**c**), TEM photograph (**d**), N_2 adsorption–desorption isotherms (**e**) and pore size distributions (**f**) of biochar, biochar-PDA-PEI and $Ti_3C_2T_x$@biochar-PDA/PEI

residual BET surface area was beneficial to the adsorption and diffusion of target pollutants.

3.2 Influence of water environmental conditions

It is well known that water environmental conditions has a marked impact on the elimination process, which may affect the zeta potential of adsorption materials as well as the species of radionuclides. In Fig. 4a, b U(VI) adsorption on $Ti_3C_2T_x$@biochar-PDA/PEI increases with an increase in pH from 2.0 to 5.0, and achieves consistent adsorption at pH 6.0–8.0. Similar to U(VI), the Cs(I) adsorption capacity gradually increased with increasing pH from 2.0 to 4.0, and then the value remained at a stable level as pH further increased to 8. This phenomenon could be explained by the electrostatic interaction. In Additional file 1: Fig. S1, the zeta potential of this adsorbent is 5.84, which implies that there would be a negative charge when pH exceeds this value. At lower

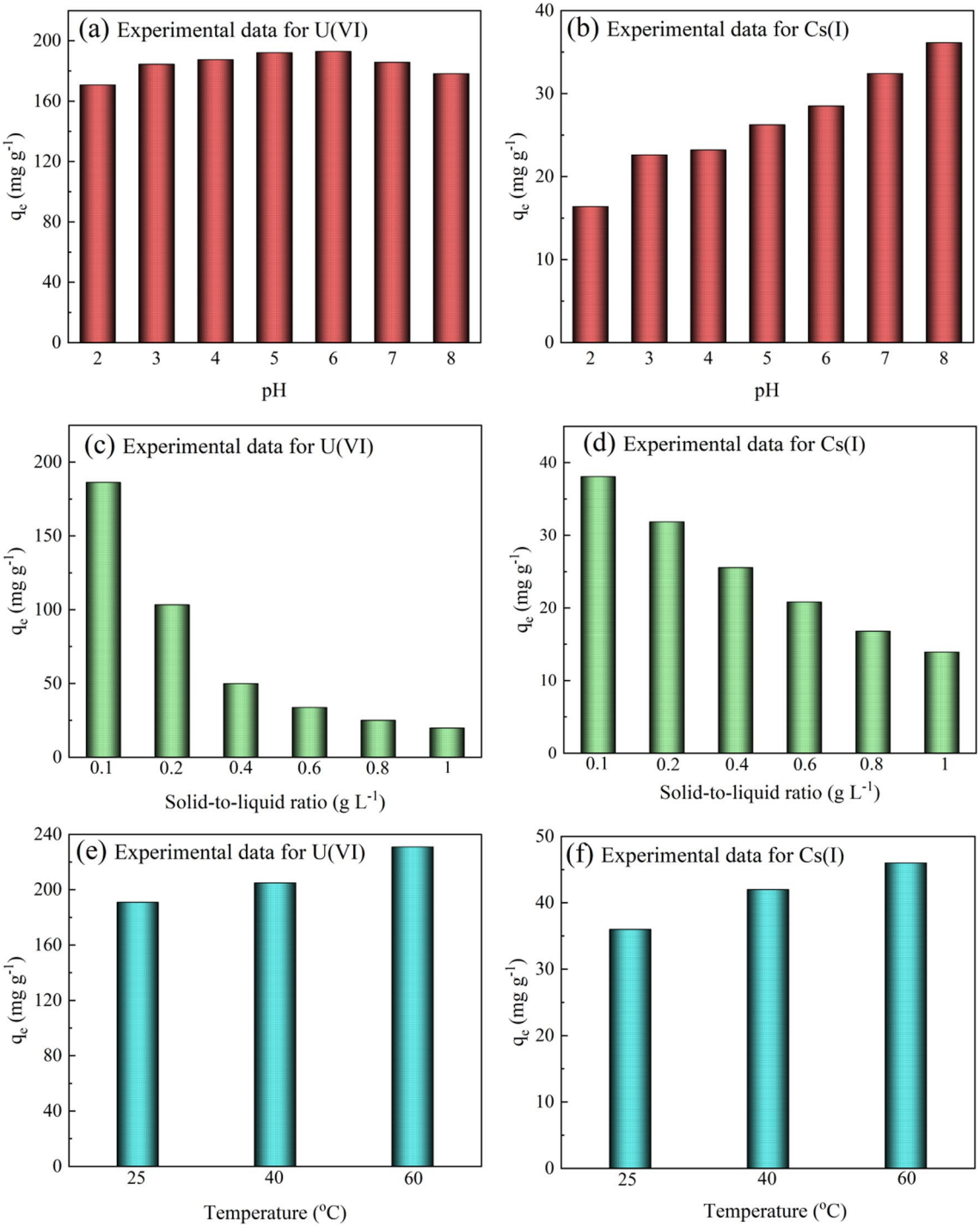

Fig. 4 Influence of water environmental conditions on adsorption of U(VI) and Cs(I) by $Ti_3C_2T_x$@biochar-PDA/PEI

pH, the competition between H^+ and radioactive cation prevented uranium or caesium ions from occupying active sites, which led to a relatively low capture amount (Yang et al. 2019). With the pH increasing, the negative charge on the $Ti_3C_2T_x$@biochar-PDA/PEI was beneficial to binding with positively charged ions through electrostatic attraction, which led to an increase in adsorption capacity. Moreover, at higher pH, the decrease in uptake amounts might be ascribed to the repulsive interaction between the negatively charged composites and the

negative radionuclides. In the actual adsorption process, the content of adsorbent was another key factor affecting the adsorption of metal ions. In Fig. 4c, d, it can be observed that the adsorption amount of $Ti_3C_2T_x$@biochar-PDA/PEI gradually reduces with solid-to-liquid ration increasing, which is owing to the lack of radionuclides in the solution compared to the amount of adsorbents (Ahmed et al. 2021a, b). In Fig. 4e, f, one can see that the adsorption can be accelerated by increasing the reaction temperature, which indicates that high temperature would enhance the adsorption force between the adsorbate and the active sites. Besides, the adsorption performance of U(VI) and Cs(I) on different adsorbents were also evaluated in this work. In Additional file 1: Fig. S2, one can find that the adsorption amount of $Ti_3C_2T_x$@biochar-PDA/PEI is higher than that of biochar and biochar-PDA/PEI. This is mainly attributable to the anchoring of MXenes nanosheets and PDA/PEI on the biochar surface, which provides abundant active sites for adsorption of U(VI) and Cs(I).

3.3 Isotherm and thermodynamic investigation

The adsorption isotherm provides valuable information about the adsorption amounts, which is important for the design and optimization of adsorption systems. In Fig. 5, one can see the sharp increase in adsorption capacities at the initial phase, which may be due to the stronger driving forces promoting the contact between radionuclides and active sites. However, adsorption efficiency maintained at a constant-level with the adsorption proceeding, which was probably due to the limited binding sites of $Ti_3C_2T_x$@biochar-PDA/PEI. To further understand the adsorption behavior, several isotherm models were adopted to fit the experimental data. Findings from the isotherm equations are summarized in Additional file 1: Table S2. Apparently, the Langmuir isotherm model could better describe the adsorption behavior than the Freundlich model as reflected by the highest determination coefficient ($R^2 > 0.99$), and the maximum adsorption amounts of U(VI) and Cs(I) were 239.7 and 40.3 mg/g, which indicated that the elimination of radionuclides onto $Ti_3C_2T_x$@biochar-PDA/PEI was a monolayer adsorption (Wang et al. 2020a, b, c). In addition, the calculated R_L values were all in the range of 0–1, which further reflected that the favorable adsorption of U(VI)/Cs(I) on $Ti_3C_2T_x$@biochar-PDA/PEI. The Vant't Hoff equation was also utilized to analyze thermodynamic issues. In Additional file 1: Table S3, it is found that the thermodynamic constants $\Delta G^\circ < 0$, which implies that the adsorption of U(VI)/Cs(I) was exothermic and spontaneous process. Both values of ΔH° and ΔS° were positive, reflecting the adsorption process was endothermic, and the removal process increased randomly. Besides, In Additional file 1: Table S4, it is noteworthy that the maximal adsorption capacity of $Ti_3C_2T_x$@biochar-PDA/PEI surpasses that of most of reported materials. This may be attributed to its unique physicochemical properties, such as the large specific surface area, abundant functional groups and high pore size, which facilitated the adsorption ability of biochar-based composites.

3.4 Kinetic studies of adsorption

It is generally acknowledged that an effective operational period and the reaction mechanism can be appropriately reveled by the adsorption kinetics. In Fig. 6, it is obvious that removal rate of U(VI)/Cs(I) is faster during the initial stage due to a large number of vacant active sites and porous structures. However, as the reaction time increased, the adsorption sites were gradually occupied, the limited active sites would make the adsorption reaction tend to equilibrium. To gain an insight into the adsorption process, four kinetic equations models were adopted for the simulation of radionuclide adsorption behaviors onto $Ti_3C_2T_x$@biochar-PDA/PEI, and the relevant formulas are displayed in Supplementary information. According to Fig. 6 and Additional file 1: Table S5, one can see that the R^2 value of the pseudo-second-order model was higher than that of the pseudo-first-order model, which implied that the adsorption behavior between the composites and U(VI)/Cs(I) was a chemical adsorption. It was also found that the β values were less than 0.1, which implied that the rate-controlling step was not the diffusion of the target ions (Li et al. 2021). In addition, mass transfer in composites would be a crucial factor in the adsorption process, therefore, the Weber-Morris Model was applied to characterize diffusion mechanism. The plots of qt vs. $t^{1/2}$ are shown in Fig. 6e, f, in which it can be found that three straight-line segments do not pass through the origin, which impliesthat the rate-limiting step was not only intra-particle diffusion but also other steps. In this work, radionuclides were first moved from the solution to outer surface of the composite material (membrane diffusion). Subsequently, these targeted contaminants diffused through the surface to enter the intra-particle diffusion step. Finally, the equilibrium stage was mainly controlled by chemical adsorption, which was corresponding to the low mass transfer driving force.

3.5 Influence of interference ions and regeneration property

Generally, natural water often contains some inorganic background constituents, which may have a potential adverse effect on the removal of U(VI)/Cs(I) by $Ti_3C_2T_x$@biochar-PDA/PEI. Thus, the adsorption selectivity was investigated in this work. As illustrated in Additional

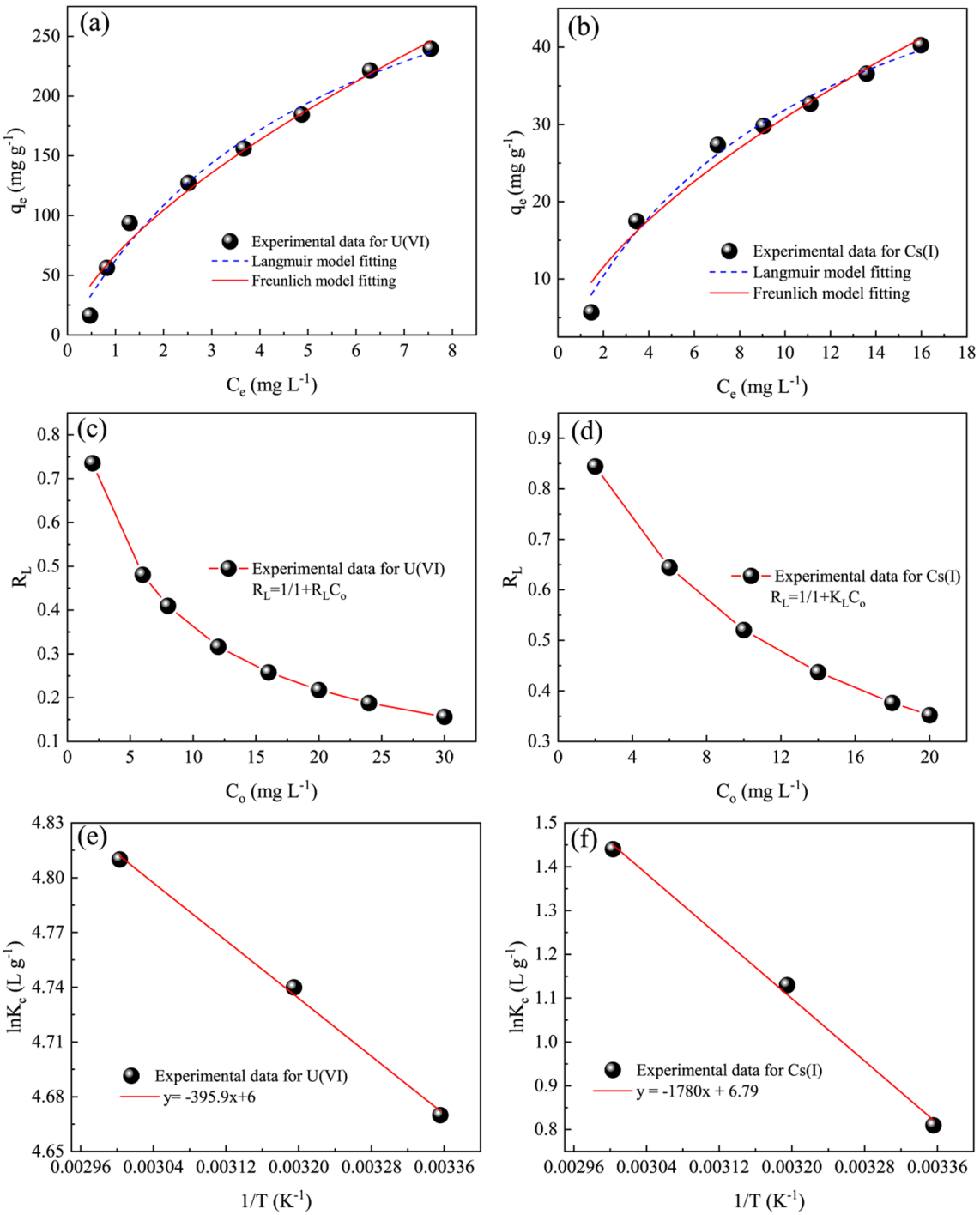

Fig. 5 The nonlinear Langmuir and Freundlich model (**a**, **b**), Langmuir separation factor (R_L) plots (**c**, **d**) and calculation of thermodynamic parameters (**e**, **f**)

file 1: Fig. S3a, there was a significant reduction in adsorption amounts in the simulated radioactive wastewater owing to the competitive relationship between U(VI) and coexisting cations. It was also found that the interference ability of metal ions in high state was higher than that in low state. This may be due to that fact that the charge value of divalent cations was higher than that of monovalent cation, so the complexation ability of divalent cations with $Ti_3C_2T_x$@biochar-PDA/PEI was stronger. In Additional file 1: Fig. S3b, this biochar based

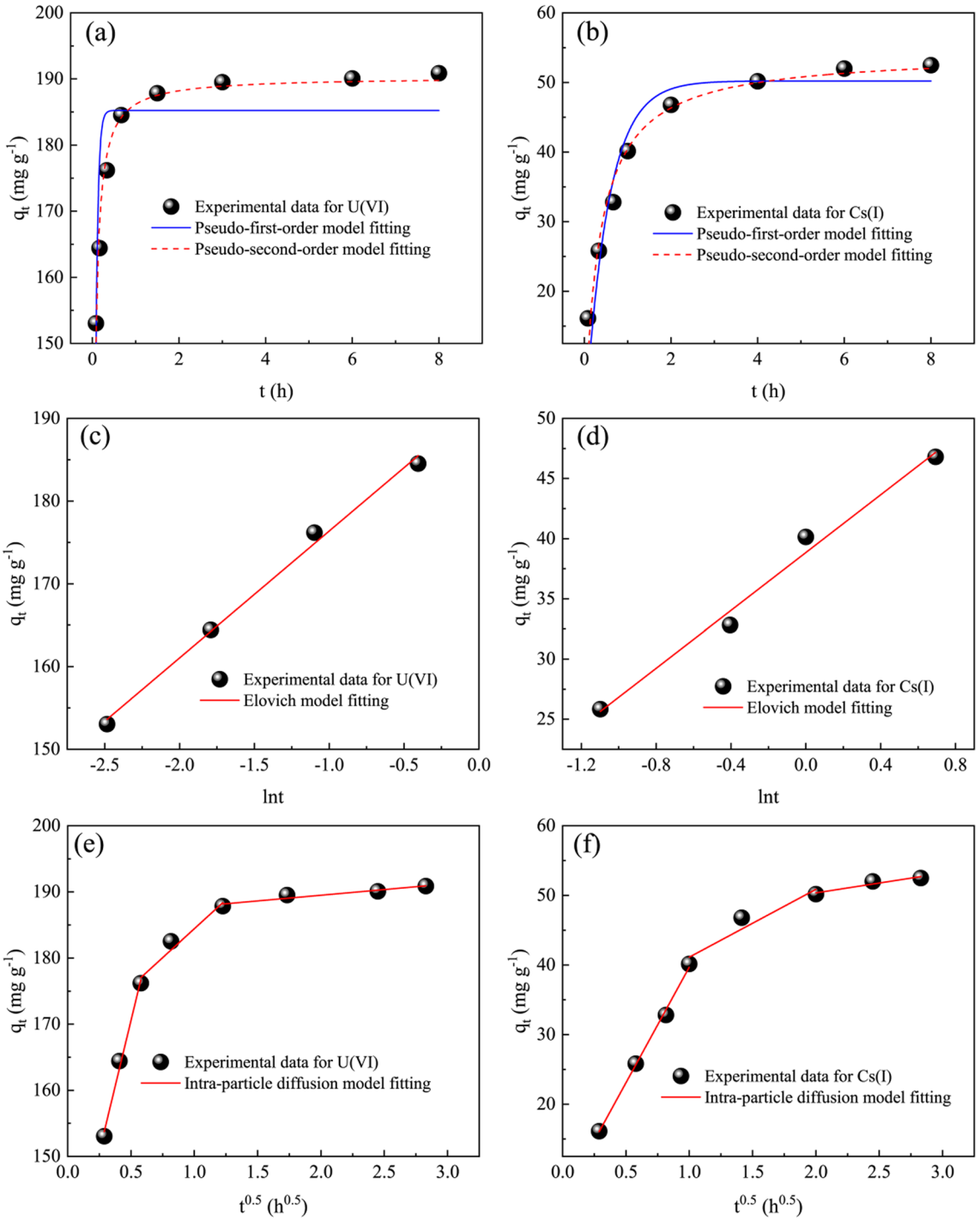

Fig. 6 Effect of contact time and adsorption kinetics plots fitted with Pseudo-first-order, Pseudo-second-order, Elovich and Intra-particle diffusion models

composite presents favorable selectivity for Cs(I) in the systems with multiple ions. This may be due to the fact that target Cs(I) ions were anchored in $Ti_3C_2T_x$@biochar-PDA/PEI with aappropriate ion size, while other metal ions had smaller radii than Cs(I), which made it difficult to form a stable chelating structure. Considering the environmental safety and economic feasibility of an adsorbent, we also evaluated the regeneration property of

$Ti_3C_2T_x$@biochar-PDA/PEI after adsorption saturation. In Additional file 1: Fig. S3c, d, it is found that the adsorption capacities maintained is maintaine 82.5% for U(VI) and 81.6% for Cs(I) after three cycles of regeneration, which indicates that this adsorbent could be well regenerated by 1 M HCl solution. These results further proved that $Ti_3C_2T_x$@biochar-PDA/PEI was not only a stable and reusable excellent adsorbent but also had a good adsorption effect on radionuclides in water environment.

3.6 Proposed adsorption mechanism

To further explain the adsorption mechanism, the fresh and spent adsorbents were elucidated by the FT-IR, SEM–EDS and XPS survey techniques. In Fig. 7a, compared with the fresh composites, the FT-IR spectra of $Ti_3C_2T_x$@biochar-PDA/PEI show a new peak at nearly 889 cm^{-1} after U(VI) adsorption, which is primarily attributed to the chemically coordinated uranyl ions (Yin et al. 2020). Meanwhile, the band at 1623 cm^{-1} was shifted to higher frequency 1630 cm^{-1} and this obvious increment could be observed after adsorption of Cs(I). These results demonstrated the interaction of hydroxyl and amino groups of $Ti_3C_2T_x$@biochar-PDA/PEI with U(VI)/Cs(I). Besides, there was another evidence shown in Additional file 1: Fig. S4, in which the surface morphology of $Ti_3C_2T_x$@biochar-PDA/PEI changed and became rough after adsorption. More importantly, the U and Cs elements were clearly observed in the SEM–EDX images, and its existence verified the incorporation of radionuclides onto the biochar-based composites.

The XPS technique was further utilized to explore the changes in chemical bonding of $Ti_3C_2T_x$@biochar-PDA/PEI before and after capture of U(VI)/Cs(I). In Fig. 7b, one can see that the typical peaks of U4f and Cs3d were detected after the adsorption processes, indicating the successful immobilization of uranium(VI) and cesium(I) on the surface of $Ti_3C_2T_x$@biochar-PDA/PEI, which was consistent with the results of SEM–EDS and FT-IR. Figure 7c shows the XPS spectra of U4f, the peaks at 392.8 eV and 381.7 eV were related to U(VI), which suggested that the absence of U(VI) reduction to U(IV) during U(VI) adsorption. In Fig. 7d, the typical peaks of Cs3d at 737.7 eV and 723.8 eV were ascribed to Cs(I), which implied that $Ti_3C_2T_x$@biochar-PDA/PEI and Cs(I) were connected by chemical bonds and there was no valence variation (see Additional file 1: Table S6). It should be pointed out that the surface of composites possessed a large amount of oxygen-containing groups, which played a vital role in the elimination process. In Fig. 7e–g, the O1s spectrum is divided into four peaks, allocated to C–OH, C=O, Ti–OH and C–O bonds at 531.1 eV, 532.6 eV, 530.6 eV and 531.8 eV, respectively. After adsorption, the content of C–OH and Ti–OH reduced to 28.77% and 13.93% for uranium(VI), while it was decreased to 23.92% and 14.72% for Cs(I). This phenomenon may be due to the fact that when the targeted pollutants were adsorbed by ligand exchange, the adsorption of radionuclides reduced the -OH on the surface of composites, resulting in a change in the content of C–OH and Ti–OH. Besides, it was also found that binding energy of N1s shifted to a lower one after adsorption (Fig. 7h), which implied that amino groups also took part in adsorption of radionuclides on $Ti_3C_2T_x$@biochar-PDA/PEI.

The DFT calculations were used to explore the adsorption process of Cs^+ and UO_2^{2+} on deprotonated $Ti_3C_2(OH)_2$ by Vienna ab initio simulation package (VASP) (Kresse and Furthmüller. 1996). The projector augmented wave (PAW) method was applied to describe the effect of core electrons on the valence electron density (Blöchl. 1994). The generalized gradient approximation (GGA) with the parametrization of Perdew-Burke-Ernzerhof (PBE) was adopted to describe the exchange correlation energy (Perdew et al. 1996). The cutoff energy for the plane wave basis sets was 500 eV. Brillouin zone was sampled by Monkhorst–Pack special k-points mesh of 4×4×1 (Monkhorst and Pack. 1976). Meanwhile, LDA+U correction was employed to better describe the electronic properties of transition metals systems. The strong on-site Coulomb repulsion of titanium (Ti) 3d electrons and uranium (U) 5f electrons were calculated, respectively, using the formalism formulated by Dudarev et al. (Dudarev et al. 1998). According to reported theoretical investigations, U values of Ti and U elements were both set to 3 eV during our calculations. All the structures were optimized until the relaxation computations reached the convergence threshold which was set to 10^{-5} eV in energy and 0.02 eV/Å in force. The adsorption energy (E_{ad}) was computed based on the following formula:

$$E_{ad} = E_{complex} - (E_{adsorbent} + E_{adsorbate}) \quad (1)$$

where the $E_{complex}$ is the total energy of Cs^+ or UO_2^{2+} adsorbed on the surface of deprotonated $Ti_3C_2(OH)_2$. The $E_{adsorbent}$ is the total energy of deprotonated $Ti_3C_2(OH)_2$ and the $E_{adsorbate}$ is the total energy of Cs^+ or UO_2^{2+} cations.

In present work, the computational model of hydroxylated Ti_3C_2 MXene material ($Ti_3C_2(OH)_2$) was built based on the literature (Wang et al. 2020a, b, c). The hydroxyl groups were introduced into the surface of bare Ti_3C_2 MXene to saturate under-coordinated Ti atoms. According to above experimental results, partial hydroxyl groups on the surface of $Ti_3C_2(OH)_2$ material were deprotonated after the deprotonation process. Thus, considering the computational cost, one and two deprotonated hydroxyl groups were present to maintain electrical neutrality for

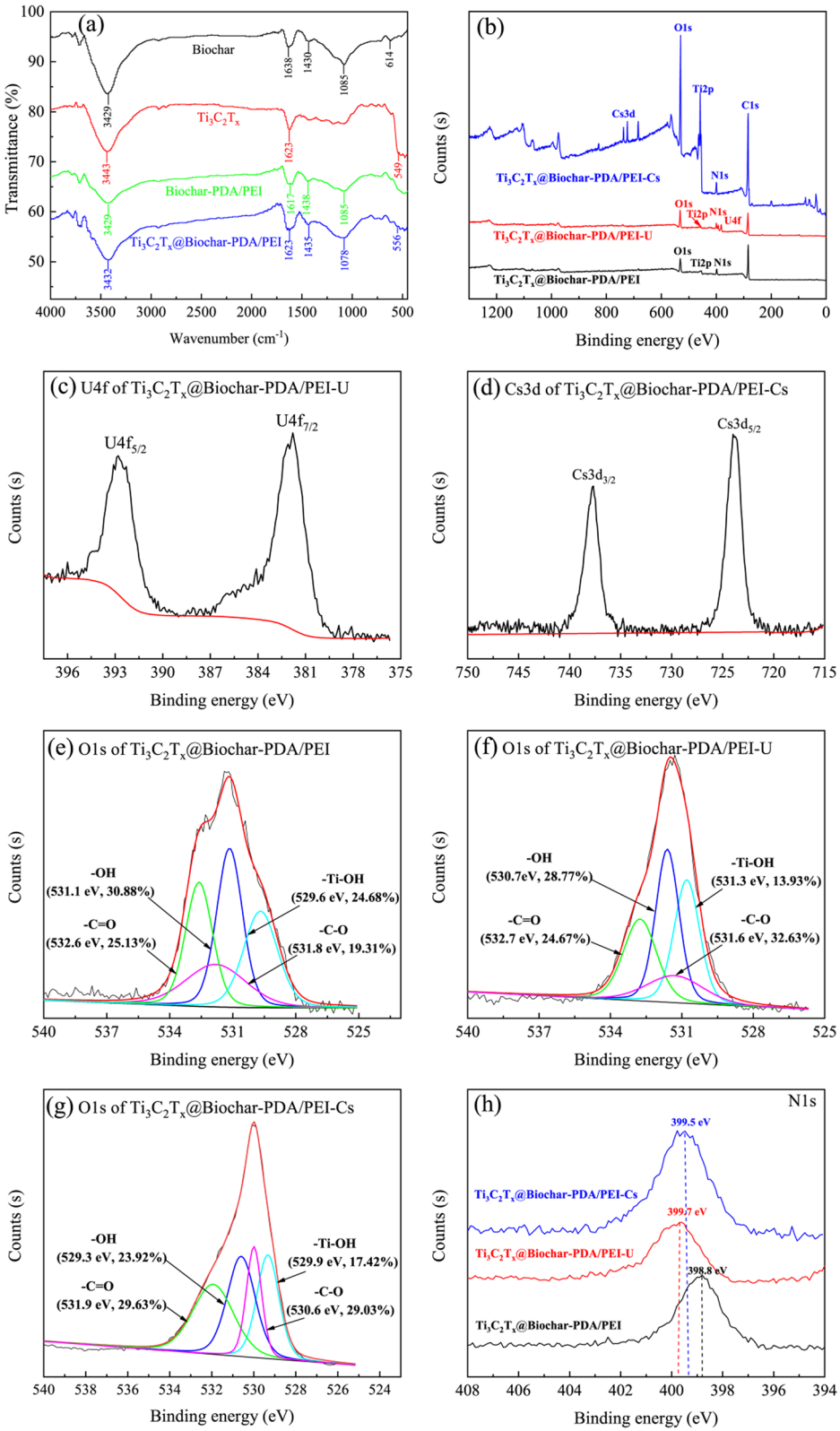

Fig. 7 FTIR spectrum (**a**), XPS survey spectra (**b**), high-resolution U4f (**c**), Cs3d (**d**), O1s (**e**–**g**) and N1s (**h**) of $Ti_3C_2T_x$@biochar-PDA/PEI before and after adsorption

cesium ion (Cs^+) and uranyl (UO_2^{2+}) systems. The unit cell parameters of bare Ti_3C_2 MXene were $a=b=3.07$ Å, $c=15.13$ Å, $\alpha=\beta=90°$, $\gamma=120°$ as shown in Additional file 1: Fig. S5a, b. A 4×4×1 supercell for deprotonated $Ti_3C_2(OH)_2$ model is displayed in Additional file 1: Fig. S5c–e. A vacuum space of 15 Å was employed to avoid the interaction between periodic images along Z-axis. The optimized complex structures for $Ti_3C_2(OH)_2$-Cs and $Ti_3C_2(OH)_2$-UO_2 are displayed in Additional file 1: Fig. S5f, g. Firstly, the Cs^+ firmly adsorbed on the top of the deprotonated oxygen atom of hydroxyl group with a Cs-O bond length of 2.84 Å. The calculated adsorption energy (E_{ad}) of Cs^+ on the deprotonated $Ti_3C_2(OH)_2$ was -17.37 kJ/mol. Besides, in the $Ti_3C_2(OH)_2$-UO_2 complex, there was strong coordination between U atom and O atom, resulting in new U–O bonds with bond lengths of 2.29 and 2.30 Å. Meanwhile, the oxygen atoms of UO_2^{2+} could also form stable hydrogen bonds (1.39 Å) with hydrogen atoms on the surface of $Ti_3C_2(OH)_2$ to further enhance the adsorption performance. Moreover, the differential charge densities of $Ti_3C_2(OH)_2$-Cs and $Ti_3C_2(OH)_2$-UO_2 complexes were also calculated. Close inspection of Additional file 1: Fig. S5h, i revealed that there was obvious charge transfer between the surface of deprotonated $Ti_3C_2(OH)_2$ and Cs^+ as well as UO_2^{2+}. Combined with the analysis of Bader charge, 0.66 and 2.09 e^- charges were transferred from the deprotonated $Ti_3C_2(OH)_2$ to Cs^+ and UO_2^{2+}, respectively. These DFT results provided a theoretical insight into the underlying adsorption mechanism of Cs^+ and UO_2^{2+}. The adsorption processes of both Cs^+ and UO_2^{2+} on the surface of deprotonated $Ti_3C_2(OH)_2$ were dominated by electrostatic interaction and the hydrogen bond was another important factor to facilitate the adsorption of UO_2^{2+}.

Based on the above analysis, elimination mechanisms of U(VI)/Cs(I) on $Ti_3C_2T_x$@biochar-PDA/PEI possibly involved three aspects (Fig. 8). (1) Electrostatic interaction. Once the targeted contaminants came into contacted with the fresh composites, the positively charged U(VI) or Cs(I) species were rapidly enriched on the surface of $Ti_3C_2T_x$@biochar-PDA/PEI by electrostatic interaction. (2) Coordination interaction. In this process, the phenol hydroxyl and amine groups were the main adsorption sites. In the process of deprotonation, the donate electrons from phenolic hydroxyl and amine groups were rapidly transferred to radionuclides, which could form stable complexes in aqueous solution. (3) Ion exchange and chelation in MXenes. A large number of Ti–OH groups existed on the surface of MXenes, which may make a great contribution to the elimination process. This was because Ti–OH groups could capture U(VI) and Cs(I) through ion exchange and chelation. Thus, this new biochar-based

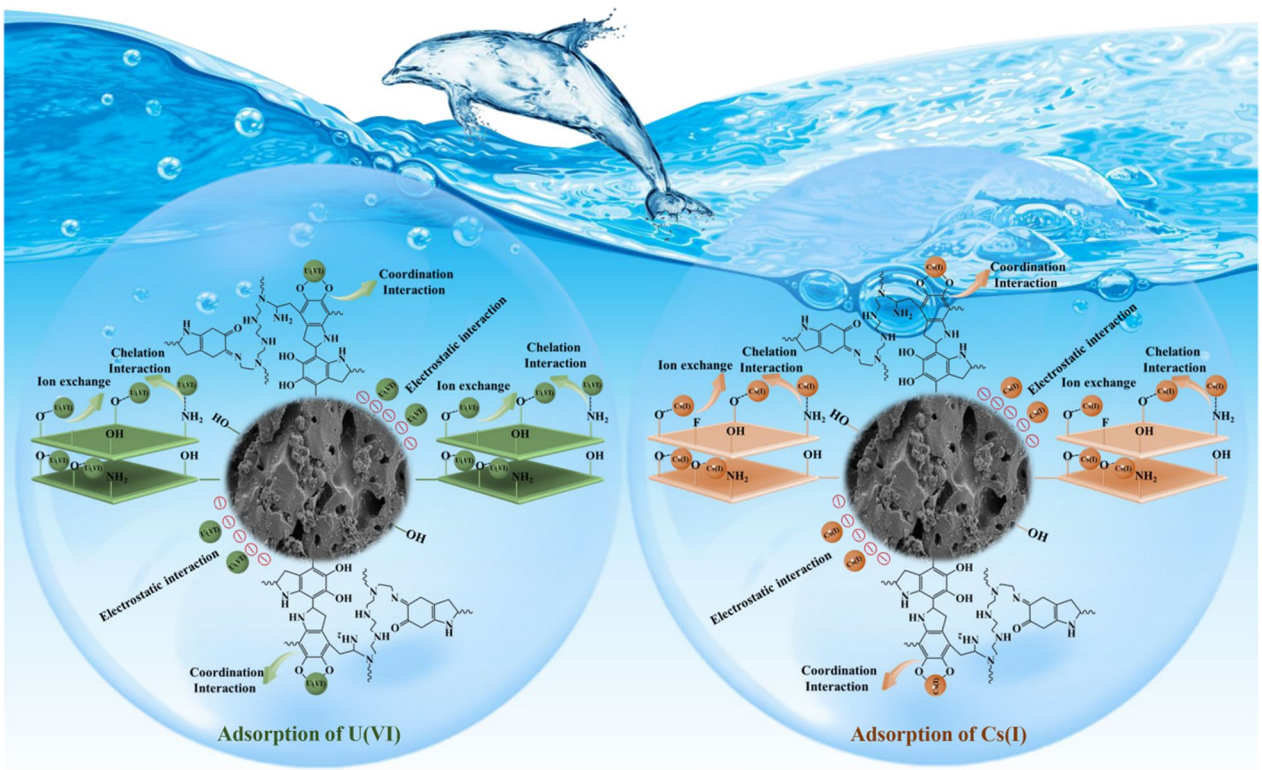

Fig. 8 Schematic diagram for proposed elimination mechanism of U(VI) and Cs(I) by $Ti_3C_2T_x$@biochar-PDA/PEI

composite material was an ideal and efficient adsorbent for radionuclide separation and enrichment.

4 Conclusion

In summary, we have successfully constructed a new type of biochar-based composite with excellent adsorption performance by a facile and cost-effective method. The characteristic results showed that the higher porosity and diverse functional groups were conducive for $Ti_3C_2T_x$@biochar-PDA/PEI to capture radionuclides. Batch experiment found that pH values and adsorption temperature normally strongly affected U(VI)/Cs(I) uptake on this composite material, whereas adsorption was only weakly inhibited by coexisting metal ions. The adsorption data were satisfactorily described by the Langmuir and Pseudo-second-order kinetics models, and the diffusion mechanism study manifested that the rate-limiting step was not only intra-particle diffusion but also other steps. Meanwhile, the maximum adsorption ability of $Ti_3C_2T_x$@biochar-PDA/PEI was higher than that of most of reported materials. Moreover, the immobilized U(VI)/Cs(I) could be easily desorbed by 1 M HCl solution, and the as-prepared material still exhibited a desirable selectivity toward radionuclides under combined system. Finally, the spectral analysis and DFT calculation demonstrated that elimination of radionuclides mainly depended on electrostatic interaction, ion exchange and chelation. Thus, this novel biochar-based material was important to the green and sustainable development of nuclear energy and environmental protection.

Supplementary Information

The online version contains supplementary material available at https://doi.org/10.1007/s42773-023-00231-z.

Additional file 1: Table S1. Summary of pore parameters of all the adsorbent. **Table S2.** Isotherms model constants for adsorption of U(VI) and Cs(I) on $Ti_3C_2T_x$@biochar-PDA/PEI. **Table S3.** Calculated thermodynamic parameters from the thermodynamic equations. **Table S4.** Comparison of U(VI) and Cs(I) elimination by $Ti_3C_2T_x$@biochar-PDA/PEI and other adsorption materials. **Table S5.** Kinetics model constants for adsorption ofU(VI) and Cs(I) on $Ti_3C_2T_x$@biochar-PDA/PEI. **Table S6.** Contents (atom %) of elements and metal ions on fresh and spent $Ti_3C_2T_x$@biochar-PDA/PEI calculated from XPS analysis. **Fig. S1.** The zeta potential of $Ti_3C_2T_x$@biochar-PDA/PEI at different pH value. **Fig. S2.** Adsorption of U(VI) and Cs(I) on biochar, biochar-PDA/PEI and $Ti_3C_2T_x$@biochar-PDA/PEI. **Fig. S3.** Influence of interference ions and regeneration property of U(VI)/Cs(I) on $Ti_3C_2T_x$@biochar-PDA/PEI. **Fig. S4.** The SEM micrographs and EDS spectrum of $Ti_3C_2T_x$@biochar-PDA/PEI-U (**a**, **c**) and $Ti_3C_2T_x$@biochar-PDA/PEI-Cs (**b**, **d**). **Fig. S5.** The (**a**) top view and (**b**) side view of the unit cell for bare Ti_3C_2 MXene. The top views (**c**, **d**) together with side view (**e**) of deprotonated $Ti_3C_2(OH)_2$ models and the deprotonated hydroxyl groups are emphasized by black circles. The optimized complex structures of (**f**) $Ti_3C_2(OH)_2$-Cs and (**g**) $Ti_3C_2(OH)_2$-UO_2. Bond lengths were in angstrom. The differential charge density of (**h**) $Ti_3C_2(OH)_2$-Cs complex and (**i**) $Ti_3C_2(OH)_2$-UO_2 complex at charge density isosurface of 0.001 and 0.01 e/Bohr^3, respectively. The purple regions indicated charge accumulation, and the pink regions represented charge depletion.

Acknowledgements
Not applicable.

Author contributions
FL: Investigation, Data curation, Writing-original draft. SW, CZ: Investigation, Project administration. BH: Writing-review & editing. All authors read and approved the final manuscript.

Funding
This research was supported by Zhejiang Provincial Natural Science Foundation of China under Grant No. LQ23B060002 and the China Postdoctoral Science Foundation under Grant No. 2021M702911.

Availability of data and materials
All data generated or analysed during this study are included in this article.

Declarations

Competing interests
The authors declare that they have no known competing financial interests or personal relationships that could have appeared to influence the work reported in this paper.

Author details
[1]School of Life Science, Shaoxing University, Huancheng West Road 508, Shaoxing 312000, People's Republic of China. [2]Key Laboratory of Ministry of Education for Advanced Catalysis Materials, Institute of Physical Chemistry, Zhejiang Normal University, Jinhua 321004, People's Republic of China. [3]MOE Key Laboratory of Resources and Environmental Systems Optimization, College of Environment and Chemical Engineering, North China Electric Power University, Beijing 102206, People's Republic of China.

Received: 11 November 2022 Revised: 15 May 2023 Accepted: 18 May 2023
Published online: 01 June 2023

References

Ahmed W, Mehmood S, Ali S, Qaswar M, Shakoor A, Chen D (2021a) Highly efficient uranium (VI) capture from aqueous solution by means of a hydroxyapatite-biochar nanocomposite: adsorption behavior and mechanism. Environ Res 201:111518

Ahmed W, Mehmood S, Núñez-Delgado A, Ali S, Qaswar M, Khan ZH, Ying H, Chen D (2021b) Utilization of *Citrullus lanatus* L. seeds to synthesize a novel MnFe2O4-biochar adsorbent for the removal of U(VI) from wastewater: insights and comparison between modified and raw biochar. Sci Total Environ 771:144955

Asada T, Sato N, Ozeki T, Ito A, Takase T (2021) Radioactive Cs removal from aqueous solutions by biochar-immobilized potassium nickel hexacyanoferrate prepared using ball mill. Int J Environ Res 15:447–455

Blöchl PE (1994) Projector augmented-wave method. Phys Rev B 50:17953–17979

Cheng Y, Wang B, Shen J, Yan P, Kang J, Wang W, Bi L, Zhu X, Li Y, Wang S, Shen L, Chen Z (2022) Preparation of novel N-doped biochar and its high adsorption capacity for atrazine based on π-π electron donor-acceptor interaction. J Hazard Mater 432:128757

Dong F, Yan L, Zhou X, Huang S, Liang J, Zhang W, Guo Z, Guo P, Qian W, Kong L, Chu W, Diao Z (2021) Simultaneous adsorption of Cr(VI) and phenol by biochar-based iron oxide composites in water: performance, kinetics and mechanism. J Hazard Mater 416:125930

Dudarev SL, Botton GA, Savrasov SY, Humphreys C, Sutton AP (1998) Electron-energy-loss spectra and the structural stability of nickel oxide: An LSDA+U study. Phys Rev B 57:1505

Fang Y, Ali A, Gao Y, Zhao P, Li R, Li X, Liu J, Luo Y, Peng Y, Wang H, Liu H, Zhang Z, Pan J (2022) Preparation and characterization of MgO hybrid biochar and its mechanism for high efficient recovery of phosphorus from aqueous media. Biochar 4:40

Gao X, ZhengY CJ, Xu H, Hui Z, Dai H, Wang H, Xia Z, Zhou J, Sun G (2022) Universal strategy for preparing highly stable PBA/$Ti_3C_2T_x$ MXene toward lithium-ion batteries via chemical transformation. ACS Appl Mater Interfaces 14:15298–15306
Guo Y, Liu X, Xie S, Liu H, Wang C, Wang L (2022) 3D ZnO modified biochar-based hydrogels for removing U(VI) in aqueous solution. Colloids Surf A 642:128606
Han Y, Gan L, Gong H, Han J, Qiao W, Xu L (2022) Photoactivation of peroxymonosulfate by wood pulp cellulose biochar/g-C_3N_4 composite for diclofenac degradation: the radical and nonradical pathways. Biochar 4:35
Hu X, Chen C, Zhang D, Xue Y (2021) Kinetics, isotherm and chemical speciation analysis of Hg(II) adsorption over oxygen-containing MXene adsorbent. Chemosphere 278:130206
Hu Y, Pan C, Liu S, Wang X, Zheng X, Hu F, Xu L, Xu G, Jian Y, Peng X (2022) Ultra-fast adsorption of radioactive-U(VI) and Cs(I) with high adsorption capacity towards CAA@MgAlFe spongy-like aerogel: mechanism and application feasibility study. J Nucl Mater 559:153463
Kresse G, Furthmüller J (1996) Efficient iterative schemes for ab initio total-energy calculations using a plane-wave basis set. Phys Rev B 54:11169
Li Q, Chen Z, Wang H, Yang H, Wen T, Wang S, Hu B, Wang X (2021) Removal of organic compounds by nanoscale zero-valent iron and its composites. Sci Total Environ 792:148546
Liu X, Wang J (2020) Electro-assisted adsorption of Cs(I) and Co(II) from aqueous solution by capacitive deionization with activated carbon cloth/graphene oxide composite electrode. Sci Total Environ 749:141524
Liu Z, Zhou Y, Guo LB, Wu Z, Zhou W (2019) Experimental and theoretical investigations of Cs^+ adsorption on crown ethers modified magnetic adsorbent. J Hazard Mater 371:712–720
Liu F, Xiang M, Wang A, Wang C, Hu B (2021) Efficient adsorption and reduction of Cr(VI) and U(VI) by nanoscale zero-valent iron supported on polydopamine-decorated SBA-15. Appl Surf Sci 568:150931
Liu F, Wang A, Xiang M, Hu Q, Hu B (2022) Effective adsorption and immobilization of Cr(VI) and U(VI) from aqueous solution by magnetic amine-functionalized SBA-15. Sep Purif Technol 282:120042
Liu F, Hua S, Xia F, Hu B (2023) Efficient extraction of radionuclides with MXenes/persimmon tannin functionalized cellulose nanofibers: performance and mechanism. Appl Surf Sci 609:155254
Lu T, Zhu Y, Kang Y, Xu J, Wang A (2021) Development of porous material via chitosan-based Pickering medium internal phase emulsion for efficient adsorption of Rb^+, Cs^+ and Sr^{2+}. Int J Biol Macromol 193:1676–1684
Lu Y, Cai Y, Zhang S, Zhuang L, Hu B, Wang S, Wang X (2022) Application of biochar-based photocatalysts for adsorption-(photo)degradation/reduction of environmental contaminants: mechanism, challenges and perspective. Biochar 4:45
Ma S, Yang H, Fu S, He P, Duan X, Yang Z, Jia D, Colombo P, Zhou Y (2023) Additive manufacturing of geopolymers with hierarchical porosity for highly efficient removal of Cs^+. J Hazard Mater 443:130161
Monkhorst HJ, Pack JD (1976) Special points for Brillouin-zone integrations. Phys Rev B 13:5188–5192
Nie X, Zhang Y, Jiang Y, Pan N, Liu C, Wang J, Ma C, Xia X, Liu M, Zhang H, Li X, Dong F (2022) Efficient extraction of U(VI) from uranium enrichment process wastewater by amine-aminophosphonate-modified polyacrylonitrile fibers. Sci Total Environ 831:154743
Peng H, He M, Zhou Y, Song Z, Wang Y, Feng S, Chen X, Zhang X, Chen H (2022) Low-temperature carbonized biomimetic cellulose nanofiber/MXene composite membrane with excellent microwave absorption performance and tunable absorption bands. Chem Eng J 433:133269
Perdew JP, Burke K, Ernzerhof M (1996) Generalized gradient approximation made simple. Phys Rev Lett 77:3865
Sun Y, Yuan N, Ge Y, Ye T, Yang Z, Zou L, Ma W, Lu L (2022) Adsorption behavior and mechanism of U(VI) onto phytic acid-modified Biochar/MoS_2 heterojunction materials. Sep Purif Technol 294:121158
Tao Q, Zhang X, Huang D, Huang G, Fan J, Peng H, Dai Y, Prabaharan K (2019) Copper hexacyanoferrate nanoparticle-decorated biochar produced from pomelo peel for cesium removal from aqueous solution. J Radioanal Nucl Ch 322:791–799
Wang L, Song H, Yuan L, Li Z, Zhang Y, Gibson JK, Zheng L, Chai Z, Shi W (2018) Efficient U(VI) reduction and sequestration by Ti_2CTx MXene. Environ Sci Technol 52:10748–10756
Wang X, Feng J, Cai Y, Fang M, Kong M, Alsaedi A, Hayat T, Tan X (2020a) Porous biochar modified with polyethyleneimine (PEI) for effective enrichment of U(VI) in aqueous solution. Sci Total Environ 708:134575
Wang Z, Liu H, Lei Z, Huang L, Wu T, Liu S, Ye G, Lu Y, Wang X (2020b) Graphene aerogel for photocatalysis-assist uranium elimination under visible light and air atmosphere. Chem Eng J 402:126256
Wang YH, Xue JM, Nie G, Guo X (2020c) Uranium adsorption on two-dimensional irradiation resistant MXenes from first-principles calculations. Phys Rev Lett 750:6
Xia M, Zheng X, Du M, Wang Y, Ding A, Dou J (2018) The adsorption of Cs(I) from wastewater using lithium-modified montmorillonite caged in calcium alginate beads. Chemosphere 203:271–280
Xu Z, Yu S, Wang J, Yu F, Xu M, Xiong J, Xiao S, Liu Y, He Y, Xu J, Zhang Z, Qiu J (2023) Synchronous construction of high sulfonic acid grafting degree and large surface area in conjugated microporous polymer adsorbents for efficient removal of uranium (VI). Sep Purif Technol 309:122953
Yang S, Li Q, Chen L, Chen Z, Pu Z, Wang H, Yu S, Hu B, Chen J, Wang X (2019) Ultrahigh sorption and reduction of Cr(VI) by two novel core-shell composites combined with Fe_3O_4 and MoS_2. J Hazard Mater 379:120797
Yin L, Hu B, Zhuang L, Fu D, Li J, Hayat T, Alsaedi A, Wang X (2020) Synthesis of flexible cross-linked cryptomelane-type manganese oxide nanowire membranes and their application for U(VI) and Eu(III) elimination from solutions. Chem Eng J 381:122744
Yu F, Zhu Z, Li C, Li W, Liang R, Yu S, Xu Z, Song F, Ren Q, Zhang Z (2022) A redox-active perylene-anthraquinone donor-acceptor conjugated microporous polymer with an unusual electron delocalization channel for photocatalytic reduction of uranium (VI) in strongly acidic solution. Appl Cataly b: Environ 314:121467
Zhang Z, Xu X, Yan Y (2010) Kinetic and thermodynamic analysis of selective adsorption of Cs(I) by a novel surface whisker-supported ion-imprinted polymer. Desalination 263:97–106
Zhang G, Li W, Chen Z, Long J, Xu C (2022) Freestanding N-doped graphene membrane electrode with interconnected porous architecture for efficient capacitive deionization. Carbon 187:86–96
Zhang J, Ma Y, Han Y, Xu K, Yao S, Shi L, Zhu M (2023) 3D porous structure assembled from MXene via breath figure method for electrochemical detection of dopamine. Chem Eng J 452:139414
Zheng H, Zhou X, Bao L, Guo J, Wang W, Huang L, Fu X (2021) Effect of the mass ratio of dopamine to salicylaldoxime on the adsorption performance of polydopamine/salicylaldoxime functionalized magnetic graphene oxide. J Solid State Chem 302:122363
Zhu X, Dong Z, Xu J, Lin S, Liu J, Cheng Z, Cao X, Wang Y, Liu Y, Zhang Z (2022) Visible-light induced electron-transfer in MoO_3 QDs/g-C_3N_4 nanosheets for efficient photocatalytic reduction of U(VI). J Alloys Compd 926:166609